Clim Dyn (2013) 40:1767–1787
DOI 10.1007/s00382-012-1660-1

Performance of Regional Integrated Environment Modeling System (RIEMS) in precipitation simulations over East Asia

Deming Zhao

Received: 18 January 2012 / Accepted: 31 December 2012 / Published online: 10 January 2013

Abstract Regional climate models (RCMs) can provide much more precise information on surface characteristics and mesoscale circulation than general circulation models. This potential for obtaining more detailed model results has motivated to a significant focus on RCMs development in East Asia. The Regional Integrated Environment Modeling System, version 2.0 (RIEMS2.0) has been developed from an earlier RCM, RIEMS1.0, at the Key Laboratory of Regional Climate-Environment for East Asia and Nanjing University. To test the ability of RIEMS2.0 to simulate long-term climate and climate changes in East Asia and to provide a basis for further development and applications, we compare simulated precipitation from 1979 to 2008 (simulation duration from 1 January 1978 to 31 December 2008) to observed meteorological data. The results show that RIEMS2.0 reproduces the spatial distribution of precipitation in East Asia but that the simulation overestimates precipitation. The simulated 30-year precipitation average is 26 % greater than the observed precipitation. Simulated upper and root soil water correlate well with remote sensing derived soil moisture. Annual and interannual variation in the average precipitation and their anomalies are both well reproduced by the model. A further analysis of three subregions representing different latitude ranges shows that there is good correlation and consistency between the simulated results and the observed data. Annual variation, interannual variation of average precipitation, and the anomalies in the three sub-regions are also well captured by the model. The model's performance on atmospheric circulation and moisture transport simulations is discussed to explore the bias between the simulation and observations. In summary, RIEMS2.0 shows stability and does well in both simulating long-term climate and climate changes in East Asia and in describing subregional characteristics.

Keywords RIEMS2.0 · Precipitation · Atmospheric circulation · Climate · Simulation

1 Introduction

Compared with General Circulation Models (GCMs), high-resolution Regional Climate Models (RCMs) can describe more detailed topography, land–sea distributions and surface vegetation (Gao et al. 2006) when simulating regional climate over East Asia. RCMs can better capture both regional forcing and large-scale forcing when nested with GCMs (Fu et al. 2000). Improvements in computing capacity and model development make possible the use of high-resolution RCMs, with finer land use and vegetation data.

RCMs were originally developed by Giorgi and Bates (1989) and Dickinson et al. (1989). They have been gradually recognized as efficient and necessary tools for studying regional climate. Since the 1980s, significant attention has been focused on RCMs development, such as RegCM (Giorgi et al. 1993a, b, 2012; Pal et al. 2007), MM5 (Grell et al. 1995; Dudhia et al. 2001), WRF (Weather Research and Forecast, Skamarock et al. 2005, 2008), REMO (Roeckner et al. 1996). Meanwhile, new mesoscale models and assimilation systems are being applied much more frequently in regional climate

D. Zhao (✉)
Key Laboratory of Regional Climate-Environment for East Asia (RCE-TEA), Institute of Atmospheric Physics, Chinese Academy of Sciences (IAP/CAS), P. O. Box 9804, Beijing 100029, China
e-mail: zhaodm@mail.iap.ac.cn

simulations, including examples in China such as RegCM (Zhao and Luo 1998; Zhang et al. 2007; Gao et al. 2001), MM5 (Tang et al. 2006), WRF (Liu et al. 2008), and REMO (Jacob et al. 2001).

The climate in East Asia is characterized by a typical monsoon climate (Fu et al. 2000). The vastness and complexity of the Asian continent, the unique configuration of the East African Highlands and the Tibetan Plateau, and the Pacific in the east all contribute to making the East Asian monsoon the most vigorous and influential of all the monsoon circulations (Annamalai et al. 1999). Meanwhile, with the rapid economic development and population growth over East Asia in recent years, there have been significant land use and cover changes, as well as increased aerosol emissions. These changes make it necessary for RCMs development to correctly reflect the East Asian Monsoon System. In Europe, RegCM3 reproduced the distributions of precipitation and surface air temperatures, as well as the centers of extremes (Giorgi et al. 2004). The model also exhibits good performance in simulating extreme climatic events in West Africa (Afiesimama et al. 2006). In East Asia, however, there are obvious biases in the location and intensity of precipitation and the surface air temperatures simulated using RegCM3 (Zhang et al. 2007; Liu et al. 2005). As RCMs are being widely used to simulate regional climate and climate changes, Chinese scientists have tried to develop RCMs more suitable to the specific conditions present in East Asia, such as RegCM_NCC (Ding et al. 1998) from the National Climate Center and the Advanced Regional Eta Model (AREM), which is based on REM (Yu 1989).

For a typical monsoon system in East Asia, the research has shown that climate and ecosystem are strongly coupled in two ways. First, the high rate of changes to the monsoon climate serves as a strong force driving variation in the ecosystem. Second, changes in the terrestrial ecosystem should significantly feedback to affect the monsoon climate. Therefore, there is a need to couple the biological component with the physical monsoon climate. The need is particularly pressing because nearly 60 % of the world's population lives in Asia and the area is undergoing rapid economic growth and continuing population increases. The anthropogenic modification of the monsoon system by industry emissions, land use/cover change and urbanization is very likely. There is a need to couple the human component with the natural monsoon system. There is also a need to couple the chemical component with the physical climate, due to anthropogenic forcing and industrialization. It is anticipated that from the point of view of earth science, a more complete monsoon system should thus be a physical, biological, chemical and social coupled system. This coupled system can be called the 'General Monsoon system' (Fu 1997; Fu et al. 2000, 2006).

This concept has been the basis for the integrated analysis and modeling theoretical framework on regional environmental systems over East Asia. Additionally, this concept is the scientific framework for MAIRS (Monsoon Asia Integrated Regional Study), a key project of the Earth System Science Partnership (ESSP). Recently, RIEMS1.0 (Regional Integrated Environmental Modeling System version 1.0, Fu et al. 2000) was developed by researchers from the START (Global Change System for Analysis, Research, and Training) Regional Center for Temperate East Asia (RCE-TEA, IAP/CAS) in 1998 based on the concept of the General Monsoon system and supported by the National Basic Research Program of China (973).

RIEMS1.0 was built on the thermodynamic framework of PSU/NCAR MM5V2 (Grell et al. 1995), into which both a land surface scheme (BATS1e, Dickinson et al. 1993) and a radiative transfer scheme (the revised CCM3, Briegleb 1992; Kiehl et al. 1997) are integrated. The model can be used to investigate the interactions between vegetation and the atmosphere, as well as the influence of aerosols on atmospheric processes. RIEMS1.0 has been widely used in regional climate studies of the East Asian monsoon system. The results from the Regional Climate Model Intercomparison Project (RMIP) have shown that RIEMS1.0 performs well (Fu et al. 2005). RIEMS2.0, based on RIEMS1.0, is now being developed by researchers from RCE-TEA and Nanjing University, China.

RIEMS2.0 is built on the thermodynamic framework of a non-hydrostatic approximation, a change from the hydrostatic approximation used in RIEMS1.0. The two models share the same land (BATS1e) and radiation (revised CCM3) schemes. To make an integrated modeling system, the Princeton Ocean Model (POM), the Atmosphere–Vegetation Interaction Model (AVIM) and a chemical model will be integrated into RIEMS2.0 in the near future. BATS1e can account for precipitation, snowmelt, canopy foliage drip, evapotranspiration, surface runoff, infiltration below the root zone, and diffusive exchange of water between soil layers. The CCM3 radiation scheme retains the same structure as that of CCM2 but includes new features such as the inclusion of aerosols and additional greenhouse gases (CH_4, NO_2) that affect short- and long-wave radiation, respectively. The results from RIEMS2.0 coupled with POM, AVIM and the chemical model show that the coupled model can improve simulations of precipitation and surface air temperatures for different subregions of East Asia. Furthermore, the relationship between human socio-economic activities and climate are accounted for through a dynamic model of land use/cover change and by incorporating the spatial distribution of CO_2 emissions (http://973.tea.ac.cn/).

RIEMS2.0 has shown good performance in simulating multiyear means and variability of climate conditions in

China (Zhao et al. 2009; Zhao and Fu 2009). RIESM1.0 occasionally overestimated the precipitation intensity for the rainfall center. However, the revised version shows better performance in the rain belt simulation, which is highly connected with the East Asian summer and winter monsoons. Ensemble simulations of two extreme climate events in China with different physical schemes and initial conditions show that the model can reproduce the extremes well (Zhao and Fu 2010). Based on the previous long-term integrations and ensemble simulations, we extend our simulated domain over East Asia. Here, we use the model to simulate climate conditions in East Asia from 1978 to 2008 to further test the simulation capabilities of RIEMS2.0 in East Asia and to evaluate the model improvements (including coupling with POM, AVIM, the chemical model, etc.) and their applications.

2 Experimental design and data

2.1 Experimental design

The model is continuously integrated from 1 January 1978 to 31 December 2008 (31 years). As described by Giorgi and Mearns (1999), RCMs spin-up time is on the order of several days for the atmospheric components but can be longer for the surface components. However, because the most hydrologically active soil region is the rooting zone (1 m depth or less), for most practical purposes the soil spin-up time can be considered to be on the order of a few seasons to a year. Therefore, the first year is used to 'spin-up' the model in the experiment and only the results for the subsequent 30 years are analyzed. The central latitude and longitude of the simulated domain are 35°N and 105°E. The horizontal mesh consists of 171 grid points in the longitudinal direction and 131 grid points in the latitudinal direction, including a 15-grid point buffer zone that is not used in the analysis. The horizontal resolution is 50 km (Fig. 1a). The air pressure at the top of the model is 10 hPa with 23 levels in the vertical dimension. This experimental design is also consistent with that of RMIP III. Based on previous work regarding RIEMS2.0′s ability to simulate regional climate in China (Zhao et al. 2009; Zhao and Fu 2009, 2010), the main physical parameterization schemes for the current experiment include the BATS1e land surface scheme, the revised CCM3 radiative scheme, the KF (Kain and Fritsch 1993) cumulus parameterization scheme, and the MRF boundary layer parameterization scheme. During the experiment, the CO_2 concentration is updated according to Forster et al. (2007). The global mean concentration of CO_2 in 2005 was 379 ppm. The average rate of increase in CO_2, determined by direct instrumental measurements over the period of 1960–2005, is 1.4 ppm year^{-1}. Between 1995 and 2005, the growth rate of CO_2 in the atmosphere was 1.9 ppm year^{-1}.

This experiment only includes the BATS1e land surface scheme and the revised CCM3 radiative scheme; no ocean or chemical models are applied. This is consistent with previous work, which is the basis of the physical parameterization scheme selection for the current experiment. A number of data fields must be supplied by RIEMS to integrate BATS1e with the main model. Additionally, some other fields must be exchanged between BATS1e and RIEMS at each time step (Dickinson et al. 1993). Variables from RIEMS, such as wind, surface air density, air temperature, water vapor mixing ratio, and precipitation, are used to compute soil, leaf and canopy temperature, soil moisture, snow cover, momentum, heat and water vapor flux by BATS1e. These variables are also returned to RIEMS as feedback.

2.2 Data

2.2.1 Driving data

Initial conditions and time-varying boundary conditions are taken from the National Centers for Environmental Prediction/National Center for Atmospheric Research (NCEP/NCAR) re-analysis dataset with a 2.5° × 2.5° resolution. The data are bilinearly interpolated into the model domain as initial and boundary conditions, and the boundary conditions are updated every 6 h. No real SST data are used, and SST data are derived from skin temperature.

2.2.2 Observed precipitation data

2.2.2.1 Observed data from meteorological stations To test the model's performance in simulating daily precipitation, observed daily precipitation between 1979 and 2008 from the China Meteorological Administration is used here. The data only cover the regions of China with 756 stations, as shown in Fig. 1b.

2.2.2.2 Global Precipitation Climatology Centre dataset The GPCC (Global Precipitation Climatology Centre) Monitoring Product (Schneider et al. 2010; Rudolf et al. 2010) uses the station database (SYNOP, CLIMAT) available via the Global Telecommunication System (GTS) of the World Meteorological Organization (WMO) at the time of analysis (2 months after the end of an analysis month). The GPCC product is recommended for use in all applications needing near real-time, high-quality gridded monthly precipitation analyses. The GPCC precipitation data cover global land area with a spatial resolution of 0.5° × 0.5°. The data are developed from the most

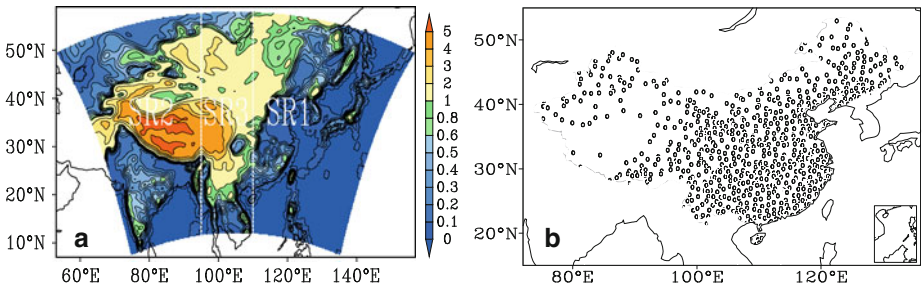

Fig. 1 Topography for the model domain without the buffer zone (unit: 10^3 m) and the three subregions (**a**), the spatial distribution of meteorological stations in China (**b**)

comprehensive database of worldwide monthly observed precipitation data from the GPCC within the framework of the German Climate Research Program (DEKLIM)-funded research project Variability Analysis of Surface Climate Observations (VASClimO). The data have been shown to express good performance on rain belt movement, connected with the East Asian summer and winter monsoons (Zhao et al. 2008; Zhao and Fu 2010). To make the comparison between the observed data and simulated results, the GPCC data are mapped to a model grid.

2.2.3 *Remote sensing derived soil moisture data*

2.2.3.1 AMSR-E daily surface soil moisture The Advanced Microwave Scanning Radiometer-Earth Observing System (AMSR-E) instrument on the NASA Earth Observing System (EOS) Aqua satellite provides global passive microwave measurements of terrestrial, oceanic, and atmospheric variables for the investigation of water and energy cycles. Soil moisture and other land surface variables are key variables in understanding land surface hydrology and in modeling ecosystems, weather, and climate. The gridded Level-3 land surface product (AE_Land3) includes daily measurements of surface soil moisture in nearly the top 1 cm of soil, vegetation/roughness water content interpretive information, brightness temperatures and quality control variables. Input brightness temperature data corresponding to a 56 km mean spatial resolution are resampled to a global cylindrical 25 km Equal-Area Scalable Earth Grid (EASE-Grid) cell spacing (Njoku 2004, http://nsidc.org/data/docs/daac/ae_land3_l3_soil_moisture.gd.html). The data between the summers of 2003 and 2008 are used in this study.

2.2.3.2 ERS scatterometer derived SWI (soil water index) Global coarse-resolution soil moisture data (25–50 km) are derived from backscatter measurements acquired with scatterometers onboard the satellites ERS-1 (1991–1996) and ERS-2 (1995–2006) and the three MetOp satellites (2006–2020). The advanced scatterometers (ASCAT) on board the meteorological operational (MetOp) platforms are the follow-on for the ERS scatterometers. Due to a change from ERS to MetOp in the sensor onboard, only soil moisture data for the years 1992 and 2006 onboard the ERS are used in this study.

The active microwave sensor acquires imagery independent of cloud cover and solar illumination. Because of the multiple viewing capabilities of the instrument, it is possible to differentiate temporal vegetation and soil moisture effects on the signal. Electromagnetic waves transmitted by scatterometers penetrate only a few centimeters into the soil surface. Therefore, the signals scattered back to the sensor only provide information about the moisture content in the soil surface layer, the so-called 'topsoil moisture'. However, the topsoil moisture may change significantly within a few hours. Furthermore, the magnitude of change depends on the amount of rainfall, the evaporation rate and the time that has passed since the rainfall event. In most applications, one is interested in the soil moisture content at a certain depth instead of the topsoil moisture. A Soil Water Index (SWI) for the top 100 cm layer was introduced based on a simple two-layer infiltration model by Wagner et al. (1999). The spatial resolution of the ERS scatterometer data is approximately 50 km, and its temporal resolution is approximately 2–3 days. The data are interpolated to 0.25° × 0.25° with a nearly 10-day temporal resolution, with approximately a 28 km spatial resolution at the middle latitudes of China. The data have been shown to reasonably depict soil moisture trends (Ceballos et al. 2005; Drusch et al. 2004; Wagner et al. 2007). These trends have also been observed in China (Zhao et al. 2006, 2008).

2.3 Monsoon related subregion analysis

Characteristics of the East Asian rainy season suggest that the Asian–Pacific summer monsoon can be divided into three regional monsoon systems: the Indian Summer Monsoon (ISM), the WNPSM (western North Pacific Summer Monsoon), and the East Asian Summer Monsoon (EASM). In between the ISM and the WNPSM is a broad transitional zone over the Indo-China Peninsula and the Yun-Gui Plateau (Wang and Lin 2002). As terrestrial precipitation is our focus, latitude-month cross-sections of rain belt movement in the three subregions are analyzed (Fig. 1). The three subregions are defined as follows: east

of 110°E (SR1, covering East Asia), west of 95°E (SR2, including the Indian subcontinent), and between 95 and 110°E (SR3, including the Indo-China Peninsula). Precipitation in the simulated regions occurs primarily in the summer. Annual and interannual variations in precipitation are analyzed to determine the model's ability to display the movement of the rain belt. As precipitation intensity varies significantly across the different subregions, the relative values of BIAS/RMSE (RBIAS/RRMSE, as defined in Eqs. 1 and 2) are discussed.

$$RBIAS = \frac{BIAS}{\bar{P}_{OBS}} \tag{1}$$

$$RRMSE = \frac{RMSE}{\bar{P}_{OBS}} \times 100\% \tag{2}$$

where BIAS is the difference between the observed data and simulated result. RMSE is the corresponding root mean square error. $\bar{P}_{OBS}$ is the observed averaged precipitation from GPCC.

3 Results

3.1 Spatial characteristics

The spatial distribution of the 30-year average (1979–2008) annual precipitation derived from the observed data (Fig. 2a) shows that precipitation is more intense in the south, ranging from the Indian subcontinent and the Indo-China Peninsula to southeast China, and then weakens in the north. This distribution is well reproduced using RIEMS2.0 (Fig. 2b). However, precipitation is generally overestimated, with the exception of southeast China, the Bay of Bengal, the southern boundary of the Tibetan Plateau, and Central Asia (Fig. 2c). The maximally overestimated subregions are located in the western Indian subcontinent, the southern Indo-China Peninsula, and the subregions covering the Tibetan plateau and Northeast Asia. East of 100°E, the simulated rain belt showed precipitation rates greater than 2 mm day^{-1} extends northward to cover Northeast Asia.

In simulations of the summer months (June, July and August, Fig. 2d–f), the subregions where precipitation is overestimated cover less area than that of annual precipitation, especially in Northeast Asia, the Tibetan plateau and the southern Indo-China Peninsula. However, the subregions where precipitation is underestimated are expanded in area, especially in southwest China and Central Asia.

In simulations of the winter months (December, January and February, Fig. 2g–i) precipitation is underestimated in southeast China, the eastern Tibetan plateau and west of the Tibetan plateau. There is a similar distribution for the subregions, with the precipitation being overestimated between annual and winter simulations, but the pattern is stronger in the winter. In the case of the subregions where precipitation is underestimated, there is a significant difference in southeast China, as well as in the eastern Tibetan Plateau and to the west of the Tibetan Plateau.

3.2 Correlation analysis

3.2.1 Monthly mean precipitation

To determine the spatial distributions of the correlation between the simulated results and the observed data for monthly average precipitation, the correlation coefficients, RBIAS and relative RRMSE for the averaged monthly results (360 months) are computed.

Correlation coefficients are mostly greater than 0.40 (Fig. 3a), especially in Northeast Asia, the northern Indian subcontinent, the Indo-China Peninsula and the eastern part of the Tibetan Plateau. However, there is a lower, even negative, correlation in Central Asia and southwest China.

The precipitation is mostly overestimated by the model, especially in the northern part of the simulated domain, as well as in the southern part of the Indian subcontinent and the Indo-China Peninsula (Fig. 2c). The precipitation is underestimated by the model in Central Asia and to the south of the Tibetan plateau, as well as in southern and southwestern China. The distributions show that the model overestimates precipitation in the north and underestimates precipitation in the south.

RRMSE, or the degree of dispersion between the observed and simulated precipitation, is greater in the middle latitudes covering the northern part of the Tibetan plateau and northern China. It is also greater in the southern Indian subcontinent and to the southwest of the Tibetan plateau (Fig. 3b). RRMSE values are lower from the northern Indian subcontinent and the Indo-China Peninsula to southeastern China.

3.2.2 Daily precipitation

Observed daily precipitation from the China Meteorological Administration (CMA) between 1979 and 2008 are used to test the model's performance to simulate daily precipitation. Thirty year mean daily precipitation is analyzed here (sample number = 365), in which daily precipitation on 29 February is averaged with 28 February for leap years. The observed data only cover the regions of China with 756 stations, which are shown in Fig. 1b. Simulated daily precipitation is resampled to station locations. Spatial distribution for the correlation coefficient, RBIAS and RRMSE at each meteorological station for 30-year mean daily precipitation, are analyzed here (Fig. 4a–c). There are similar distributions for

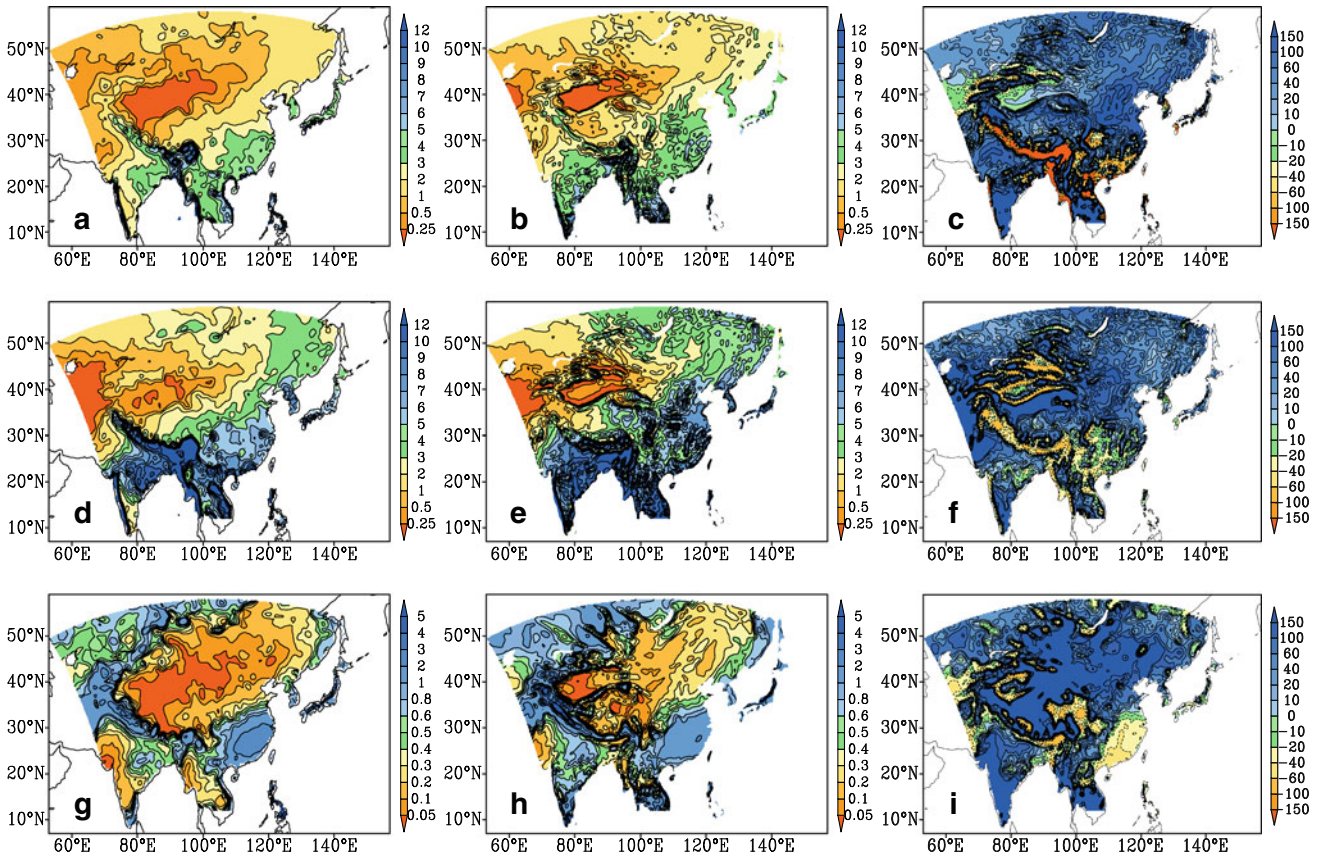

Fig. 2 Observed (**a**, **d**, **g**, unit: mm day^{-1}), simulated (**b**, **e**, **h**, unit: mm day^{-1}) and RBIAS (**c**, **f**, **i**, unit: %) values for monthly average precipitation at annual (**a**, **b**, **c**), summer (**d**, **e**, **f**) and winter (**g**, **h**, **i**) time scales between 1979 and 2008

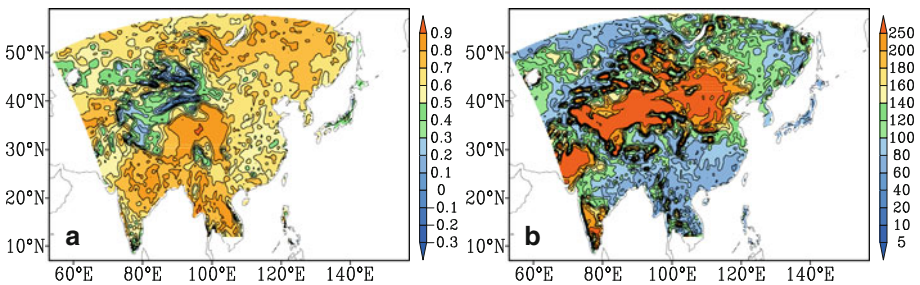

Fig. 3 The spatial distributions of correlation coefficients (**a**) and RRMSE (**b**, unit: %) between the observation and simulation for monthly average precipitation from 1979 to 2008

the correlation analysis between daily and monthly mean precipitation. However, there are higher correlation coefficients and lower RBIAS and RRMSE values for daily precipitation than for the monthly mean results. This may result from two aspects. First, the observed data used has a greater spatial resolution than the GPCC data. Second, the model expresses accurately the variation in daily precipitation.

3.3 Annual and seasonal variations

3.3.1 Across the full East Asian region

Simulated and observed monthly average precipitation shows a higher correlation (0.92) in February and lower correlation (0.45) in July (Fig. 5a). Additionally, RRMSE and RBIAS are both higher in the spring and lower in the summer and autumn, which means that the simulated precipitation is closer to the observed data in the summer and autumn.

An analysis of anomalies found that the consistency of anomaly symbol (CAS) is consistently greater than 0.68 and reaches a maximum in February (Fig. 5b). Correlations between the simulated and observed precipitation are stronger in February and are not as strong in July. RMSE of the anomaly fields is greater in the summer and lower in the winter, thus showing better performance in winter.

To further disclose the subregional characteristics for the annual variations of average precipitation, the model's

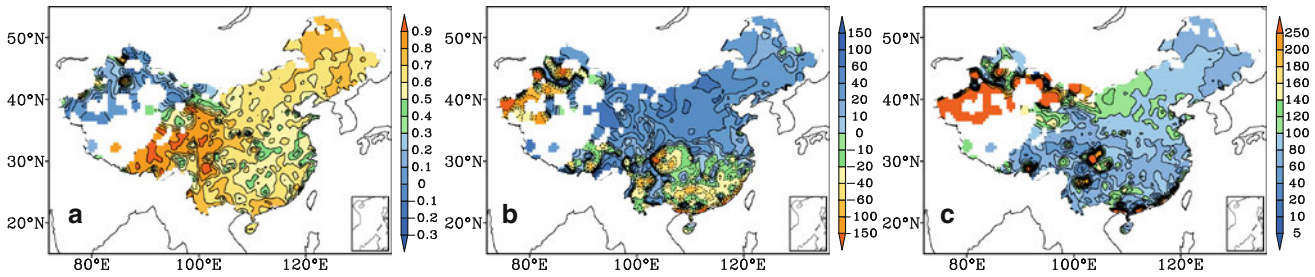

Fig. 4 The correlation analysis on daily precipitation between the observation and simulation for the years 1979 and 2008 (**a** correlation coefficient; **b** relative bias, unit: %; **c** relative RMSE, unit: %, *white areas* for no value)

performance in simulating different precipitation intensities is analyzed. Across the full East Asian region, the precipitation intensity is divided into five ranges: less than 0.568 mm day^{-1}, 0.568–1.038 mm day^{-1}, 1.038–1.706 mm day^{-1}, 1.706–3.536 mm day^{-1} and greater than 3.536 mm day^{-1} (Fig. 5c–g). There are equal grid numbers for the different precipitation intensities. In general, the model exhibits good correlations for the subregions with different precipitation intensities, except for the negative correlation observed in July for the subregions with a precipitation intensity between 1.706 and 3.536 mm day^{-1}. RRMSE/RBIAS is greater from June to December for the weaker precipitation intensity than for the stronger one, in which a negative RBIAS for the subregions with the precipitation intensity greater than 3.536 mm day^{-1} is observed. The simulated results for the stronger precipitation intensity are closer to the observed data and exhibit less dispersion.

3.3.2 In the subregions

To assess the model's ability to capture the movement pattern of the rain belt, annual variations in both simulated and observed precipitation are calculated in each of the three subregions (SR1, SR2 and SR3).

In SR1, which is highly connected with the East Asia Monsoon (EAM), the latitude-month cross-section of rain belt movement (Fig. 6a, b) shows that the model can generally grasp the movement of the rain belt and represent the oscillation of the EAM. Precipitation is generally overestimated by the model, except in southeastern China. RBIAS reaches a maximum in northern China in the late winter and early spring (Fig. 6c). In southeast China, the model underestimates precipitation except in the late summer and early autumn. Notably, there is a stronger positive bias (absolute value) in late spring and early summer precipitation downstream of the Yangtze River Valley due to the strong intensity of precipitation in that area.

In SR2, which is highly connected with the Indian Monsoon (IM) in the lower latitudes, the latitude-month cross-section of rain belt movement (Fig. 6d, e) demonstrates that the model generally captures the movement of the rain belt in terms of both intensity and location. The oscillation of the IM, which results in precipitation between May and October and maximum precipitation in the summer, is well represented by the model. However, the model generally overestimates precipitation, especially in the winter, in both the lower latitudes and in the northern Tibetan plateau between 36°N and 38°N (Fig. 6f). Meanwhile, the model underestimates precipitation in the north Indian subcontinent and the southwestern Tibetan plateau between 20 and 34°N, especially in the summer. North of 40°N, precipitation is underestimated in the late summer and early autumn.

In SR3, which is highly connected with Indo-China Peninsula Monsoon in the lower latitudes (Fig. 6g, h), the latitude-month cross-section shows that the model can capture the rain belt movement in this subregion. However, precipitation is overestimated in areas north of 30°N, especially from winter to spring and in September (Fig. 6i). Precipitation is also overestimated in the lower latitudes, particularly in the winter and early spring months. In the northern Indo-China Peninsula and in southwest China, the model generally overestimates spring and late winter precipitation and underestimates June to December precipitation.

3.4 Interannual variations

3.4.1 Across the full East Asian region

Analysis of the relationship between interannual variation of simulated and observed average precipitation from 1979 to 2008 shows that the correlation coefficient between simulated and observed variation is 0.37, with an RRMSE and RBIAS of 26.8 and 26.2 %, respectively. On average, the simulated precipitation is 26 % greater than observed precipitation. For the corresponding anomaly (Fig. 7a), the consistency of the anomaly symbol is 53 %, and the correlation coefficient is 0.30, suggesting that the model can generally grasp major anomalies.

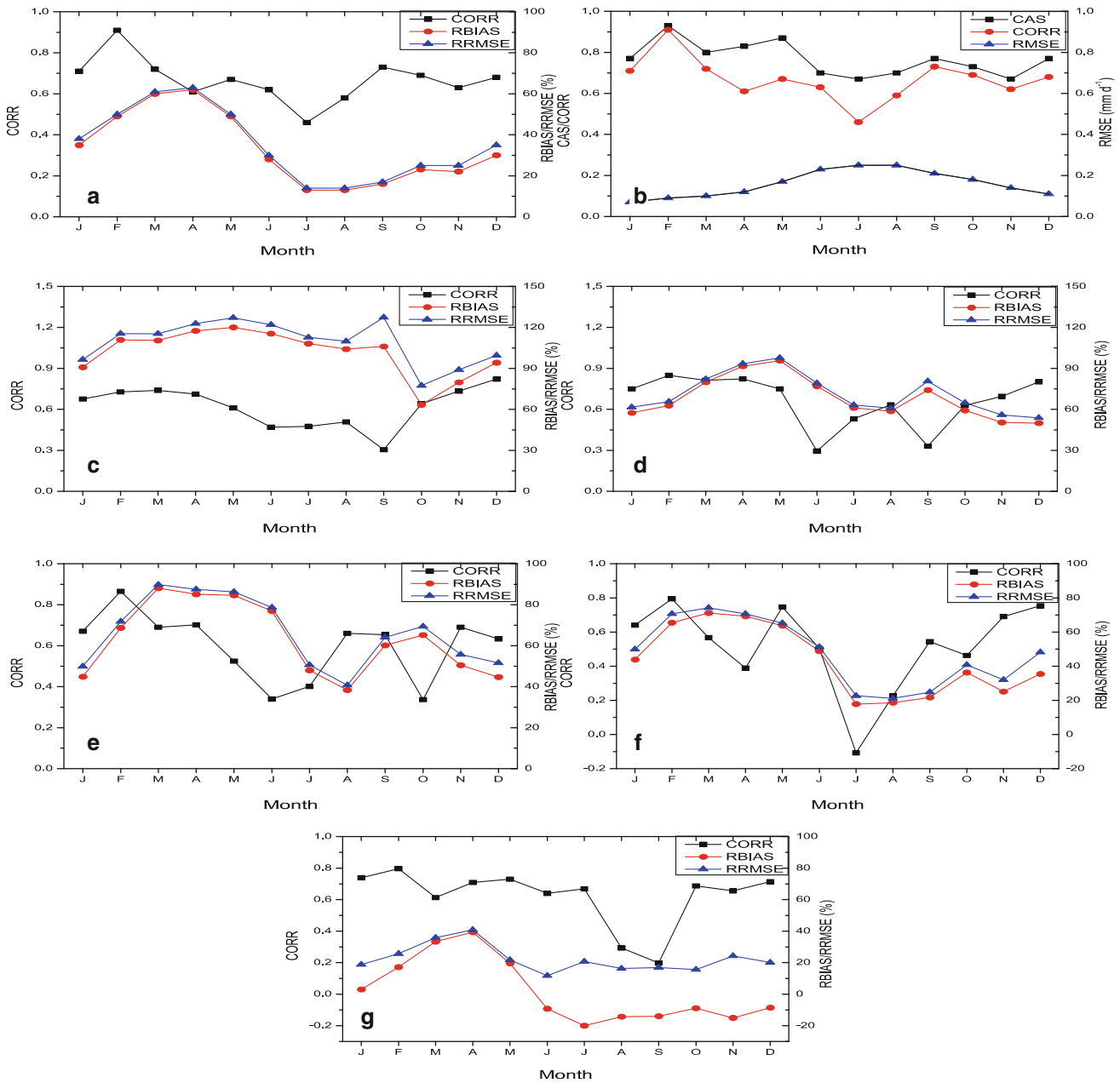

Fig. 5 Annual variations of correlation coefficients, RBIAS, RRMSE/RMSE and the consistency of the anomaly symbol (CAS) for monthly average precipitation (**a** the full simulated domain; **c**–**g** for the subregions with different average precipitation rates, **c** less than 0.568 mm day^{-1}; **d** 0.568–1.038 mm day^{-1}; **e** 1.038–1.706 mm day^{-1}; **f** 1.706–3.536 mm day^{-1}; **g** greater than 3.536 mm day^{-1}) and the anomalies (**b**) for the entire simulated domain

To disclose subregional characteristics for the interannual variations in the anomaly, the model's performance in simulating different precipitation intensities (same definition as Sect. 3.3.1) is analyzed (Fig. 7b–f). The correlation coefficients for the different precipitation rates are 0.60, 0.46, 0.41, 0.19 and 0.55. The corresponding CASs are 67, 77, 63, 50 and 77 %. The model shows good correlation and can grasp the consistency of the anomaly symbol, except for the subregions where the precipitation intensity is between 1.706 and 3.536 mm day^{-1}.

3.4.2 *In the subregions*

3.4.2.1 Average precipitation Observed interannual variations in precipitation show a similar distribution among three subregions, with variation being higher in the south and lower in the north. The model can generally reproduce this distribution (figures omitted). Correlation coefficients between the simulated and observed precipitation for each subregion are nearly equal, at 0.93, 0.89 and 0.92 in SR1, SR2 and SR3, respectively (Table 1). The

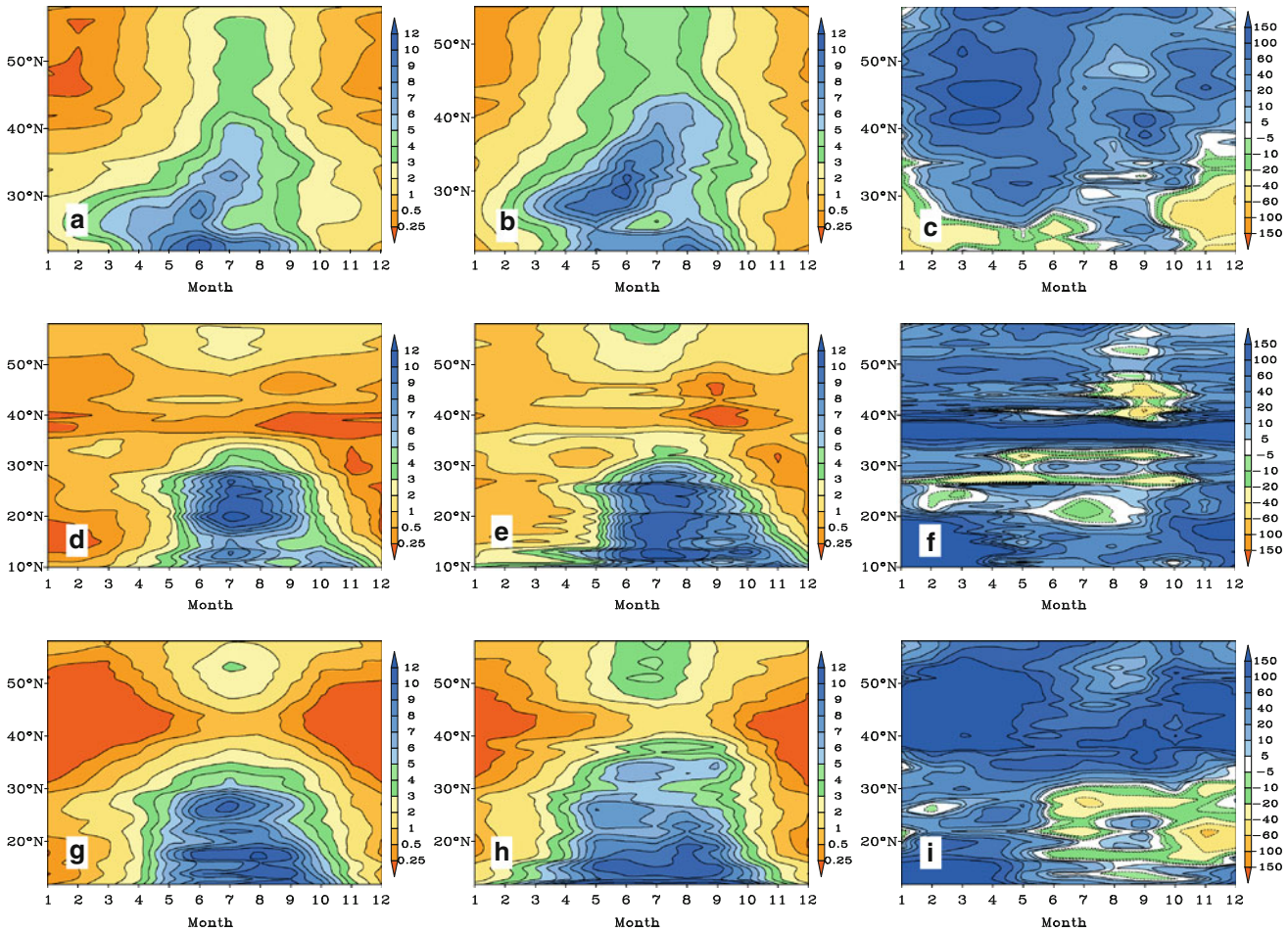

Fig. 6 Latitude-month cross-sections of annual variation for precipitation in SR1 (**a**, **b**, **c**), SR2 (**d**, **e**, **f**) and SR3 (**g**, **h**, **i**) from 1979 to 2008 (**a**, **d**, **g**, observed; **b**, **e**, **h**, simulated; unit: mm day^{-1}; **c**, **f**, **i**, RBIAS, unit: %)

corresponding RRMSE/RBIAS values are 30 %/18 %, 58 %/34 % and 41 %/26 %, indicating lower dispersion between observed and simulated precipitation in SR1 and higher dispersion in SR2.

In SR1, the difference between the observed and simulated data is negative in the south and positive in the north with greatest RBIAS values observed north of 40°N (Fig. 8a). This result indicates that precipitation is underestimated in southern China, while the rain belt extends farther north in the simulation than is apparent in the observed data. In SR2, there are two precipitation belts overestimated: one located in southern India and one in the 36–39°N region (Fig. 8b). There are both positive and negative biases between the two RBIAS belts. In SR3, the precipitation is heavily overestimated at 33–45°N and less overestimated in southern Indo-China (Fig. 8c). Between 18 and 33°N, RBIAS is both positive and negative.

3.4.2.2 Precipitation anomalies Spatial distributions for the interannual variations of precipitation anomalies also show consistency in the three subregions between 1979 and 2008 (Fig. 9). The spatial correlations for the three subregions are almost equal, at 0.34, 0.37 and 0.36 for SR1, SR2, and SR3, respectively.

3.5 Comparison for soil moisture between observed and simulated results

Spatial distributions for average soil moisture between the observed and simulated data in the summer are shown in Fig. 10. The upper soil water data are based on surface soil water and represents the water in the upper layer 0–10 cm, while the rooting soil water data are based on the rooting zone depth according to land cover/vegetation type (Dickinson et al. 1993).

For the SWI and simulated soil water, good spatial consistency can be found between the remote sensing-derived data and the simulated results. Soil moisture is greater in southwestern China and the Indo-China Peninsula, as well as in northeastern Asia, and lower in northwestern China and Central Asia. AMSR-E and simulated soil water exhibit a similar distribution to that between SWI

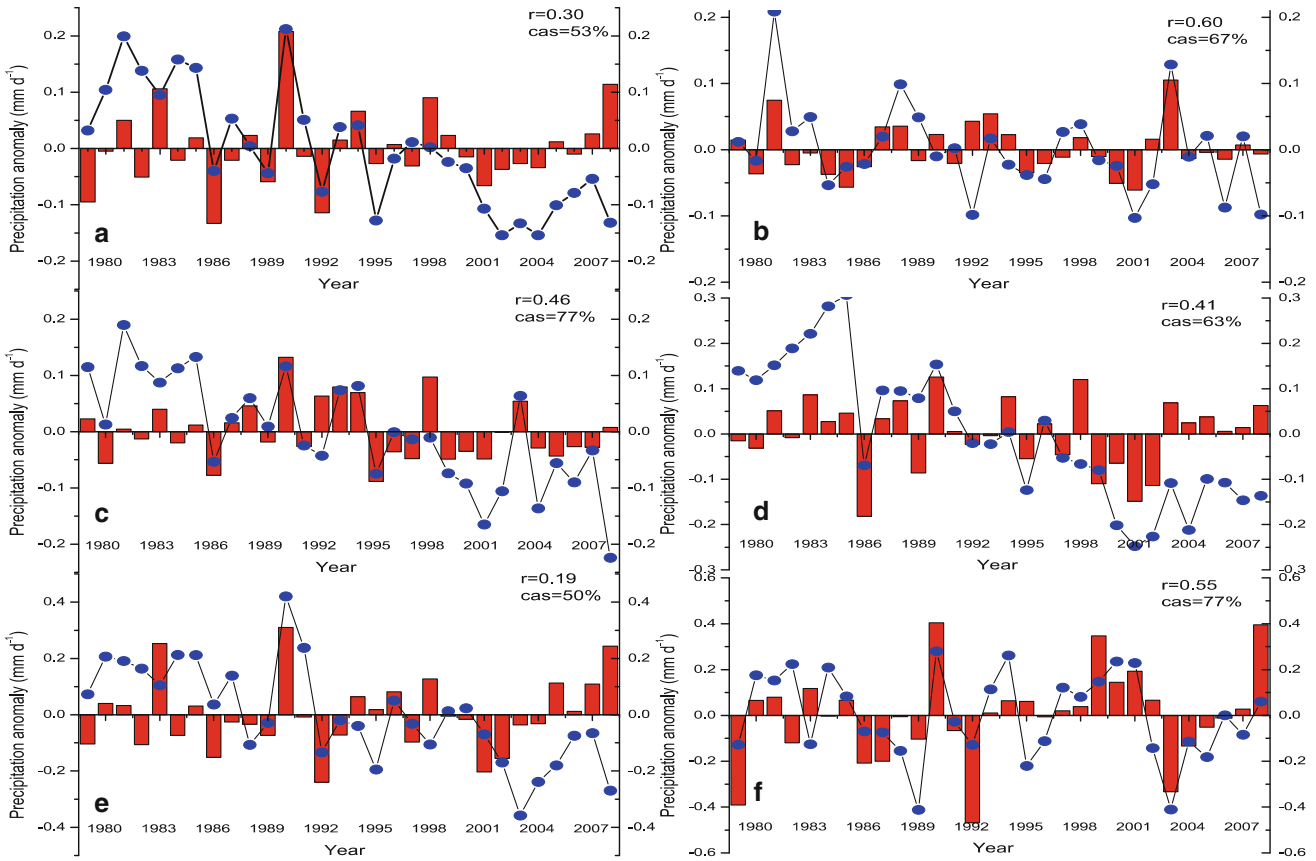

Fig. 7 Observed (*bar*) and simulated (*line*) interannual variation in precipitation anomalies (**a** the entire simulated domain, **b–f** for the subregions with different average precipitation rates, **b** less than 0.568 mm day^{-1}; **c** 0.568–1.038 mm day^{-1}; **d** 1.038–1.706 mm day^{-1}; **e** 1.706–3.536 mm day^{-1}; **f** greater than 3.536 mm day^{-1})

Table 1 Correlation coefficients, RMSE (RRMSE) and BIAS (RBIAS) of interannual variation for average precipitation and anomalies between simulated and observed data (unit: mm day^{-1})

	Average			Anomaly		
	SR1	SR2	SR3	SR1	SR2	SR3
CORR	0.93	0.89	0.92	0.34	0.37	0.36
RMSE	1.04	1.14	0.95	0.33	0.63	0.30
RRMSE (%)	30	58	41			
BIAS	0.61	0.66	0.59			
RBIAS (%)	18	34	26			

and simulated upper soil water. However, the spatial consistence between AMSR-E and simulated upper soil water is lower than that between SWI and simulated upper soil water. The less spatial consistence may result from AMSR-E derived surface soil water being highly affected by rainfall, the evaporation rate and the time that has passed since the rainfall event.

For simulated upper and root soil water between 1992 and 2006, the spatial correlation coefficients with SWI are 0.66 and 0.71, respectively. The corresponding correlation coefficients for simulated results for AMSR-E between 2003 and 2008 are 0.64 and 0.57. There is high consistency between the observed and simulated data. Meanwhile, as the SWI data represent the soil water for the 100 cm soil layer and the AMSR-E data represent the 1 cm surface soil water content, the higher correlations for root soil water with SWI and for upper soil water with AMSR-E indicate that the model can correctly express the soil moisture distribution at different layers.

3.6 Bias analysis

The model can generally reproduce intensity, spatial distribution and annual and interannual variation for precipitation over East Asia and its subregions. However, there are biases between the simulated results and observed data, which are partly revealed by the model's performance on atmospheric circulation and moisture transport simulations in the summer and winter.

3.6.1 In summer

3.6.1.1 Precipitable water and specific humidity For precipitable water (PWAT, Fig. 11a–c), the bias shows

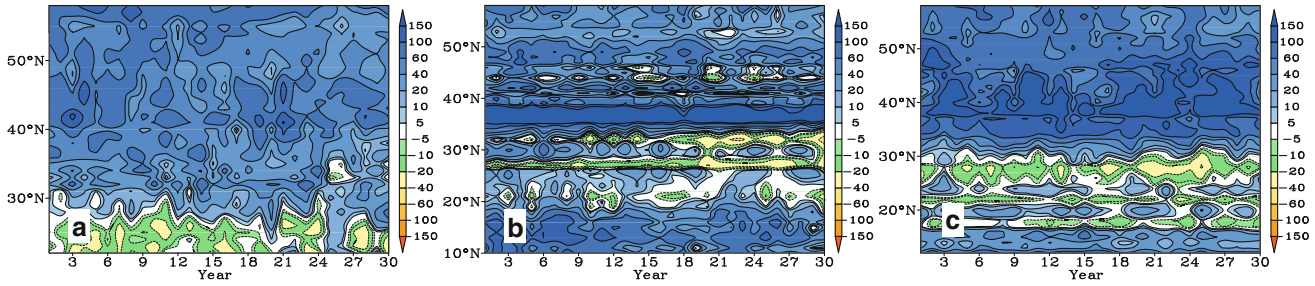

Fig. 8 Latitude-year cross-section of interannual variation in the RBIAS between observed and simulated precipitation in SR1 (**a**), SR2 (**b**) and SR3 (**c**) from 1979 to 2008 (unit: %)

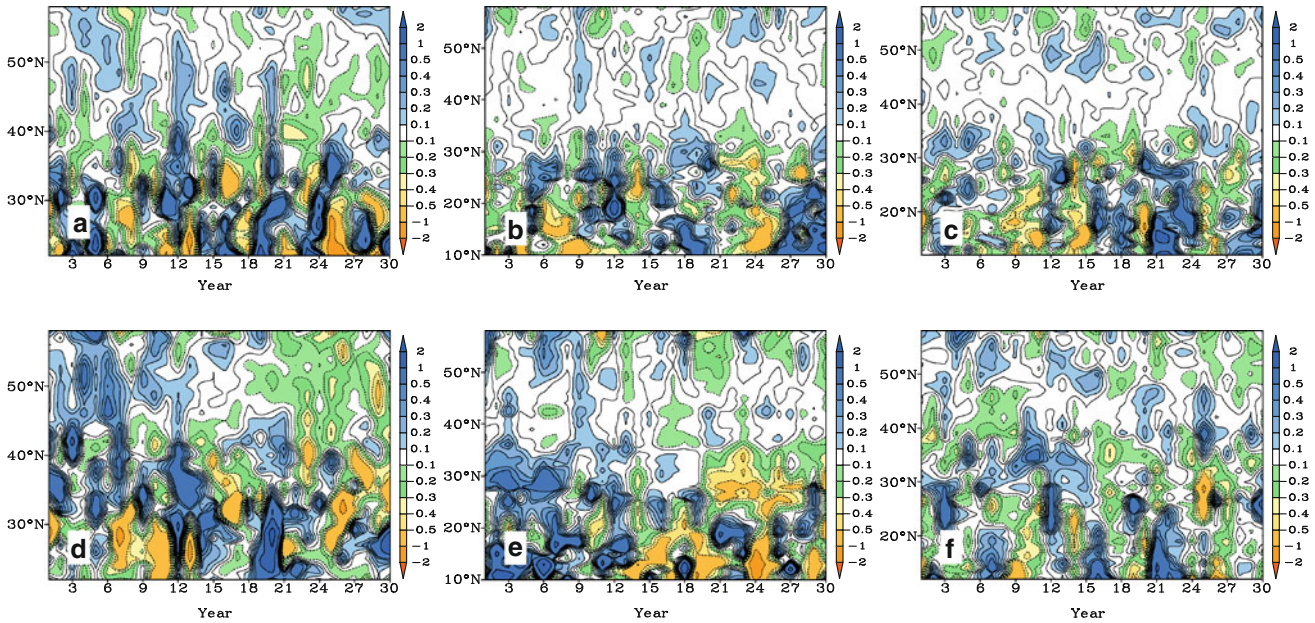

Fig. 9 Latitude-year cross-section of interannual variation in precipitation anomalies in SR1 (**a**, **d**), SR2 (**b**, **e**) and SR3 (**c**, **f**) from 1979 to 2008 (**a**, **b**, **c**, observed; **d**, **e**, **f**, simulated, unit: mm day^{-1})

contrary characteristics over eastern China, being positive in the north and negative in the south. Additionally, the bias is positive over the Indian subcontinent and negative over the Indo-China Peninsula. It is worth noting that there is a strong positive bias in the south boundary of the Tibetan Plateau for the simulated PWAT.

For specific humidity at 850 hPa (Fig. 11d–f), the bias has a similar distribution to that of PWAT in eastern China. There is an obvious positive bias in northern China and a negative bias in southeast China, the western Pacific and the Indo-China Peninsula. This bias is lower in the Indian subcontinent.

3.6.1.2 Pressure-latitude cross-section for wind field The pressure-latitude cross-section along the 115°E axis for the zonal and meridional winds in the summer (Fig. 12) are analyzed to determine the model's performance in East Asian summer and winter monsoon simulations.

In the summer, the pressure-latitude cross-section is occupied by the westerly winds across the whole troposphere along the latitude, except for the easterly winds above 600 hPa in the low latitudes (Fig. 12a). The meridional winds in the low troposphere are southerly winds in the middle and low latitudes, and northerly winds in the middle and high latitudes. Consistently northerly winds are observed in the upper troposphere (Fig. 12d). The model can generally grasp the vertical distribution of the wind (Fig. 12b, e). However, there are differences between the observed data and the simulated results.

For the zonal winds, the subtropical westerly jet at 200 hPa in the simulation is stronger than that observed, with the center moving northward; the corresponding westerly winds in the low troposphere are also stronger in the middle latitudes (Fig. 12c). For the meridional winds, the simulated center of the strong northerly winds is to the

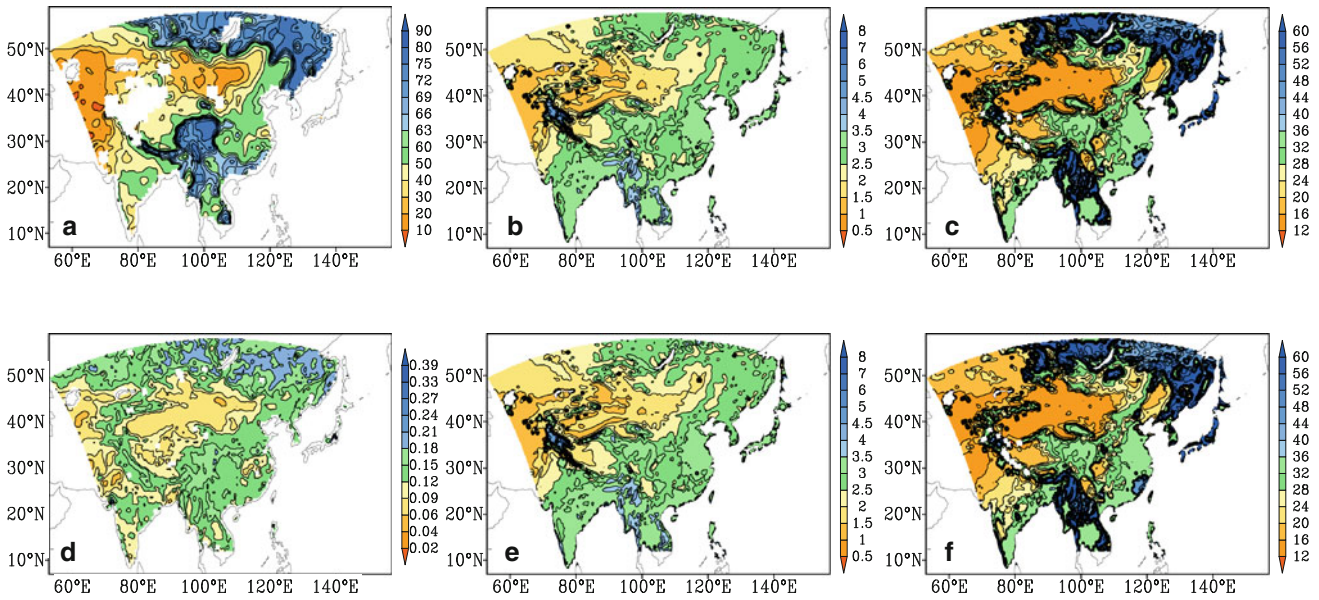

Fig. 10 The spatial distributions of average soil moisture between remote sensing derived data (**a** SWI, unit: %, **d** AMSR-E, unit: g cm^{-3}) and simulated results (**b** and **e** for the upper soil water, **c** and **f** for the rooting soil water, unit: cm H_2O) in the summer for two time periods (**a–c** for the years 1992 and 2006, **d–f** for the years 2003 and 2008, *white areas* for no value)

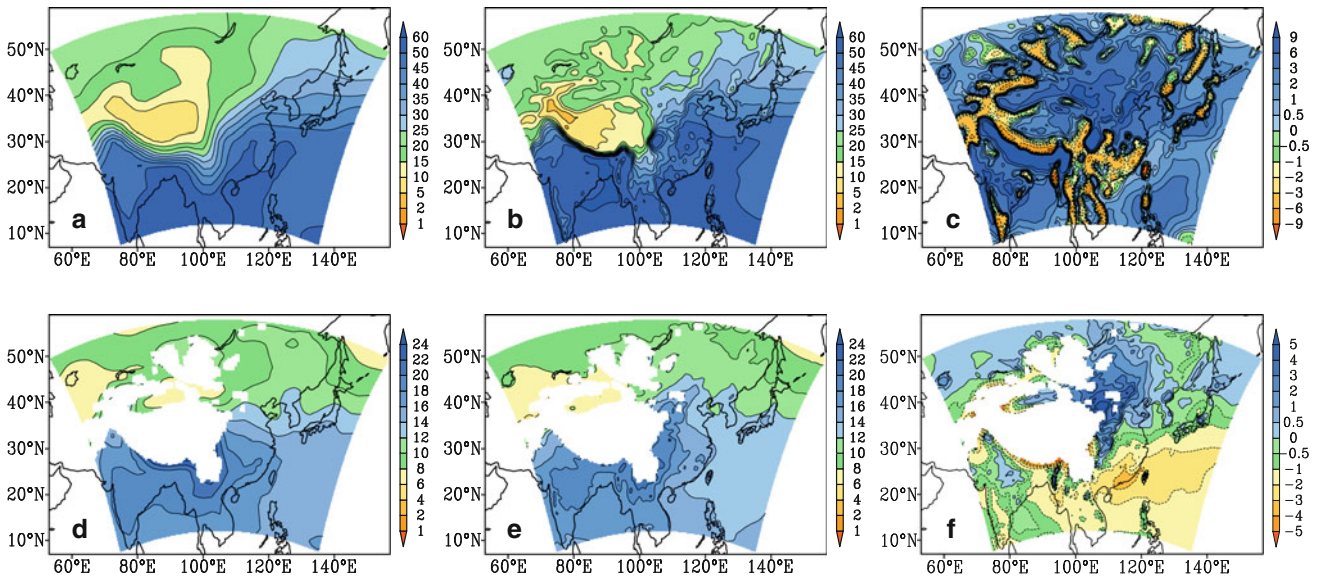

Fig. 11 The spatial distributions of average precipitable water (**a–c**, unit: cm) and specified humidity (**d–f**, unit: 10^{-3} kg kg^{-1}) at 850 hPa (*white areas* for topography above 850 hPa) in the summer between 1979 and 2008 [**a**, **d** observed, **b**, **e** simulated, **c**, **f** bias (simulated–observed)]

north and in the lower layer of the observed data, with stronger southerly winds in the low troposphere (Fig. 12f).

The simulated strong subtropical westerly jet and northward of the wind center in the upper troposphere result in stronger westerly and southerly winds in the low troposphere. Therefore, the simulated summer monsoon circulation is stronger than the observed one and has a potential effect on moisture transport.

In East Asia, the rain belt movement is highly connected by summer monsoon-affected atmosphere circulation and moisture transport. The differences in the meridional and zonal winds at 850 hPa between the observation and simulation, as well as moisture flux, will be discussed below.

3.6.1.3 Subtropical westerly jet Spatial distributions of the 30-year average subtropical westerly jet and its bias over East Asia show that the bias is positive in India, the Bay of Bengal and Northeast Asia; while negative from southeast to northwest China and Central Asia (Fig. 13a–c). The bias displays positive–negative–positive spatial

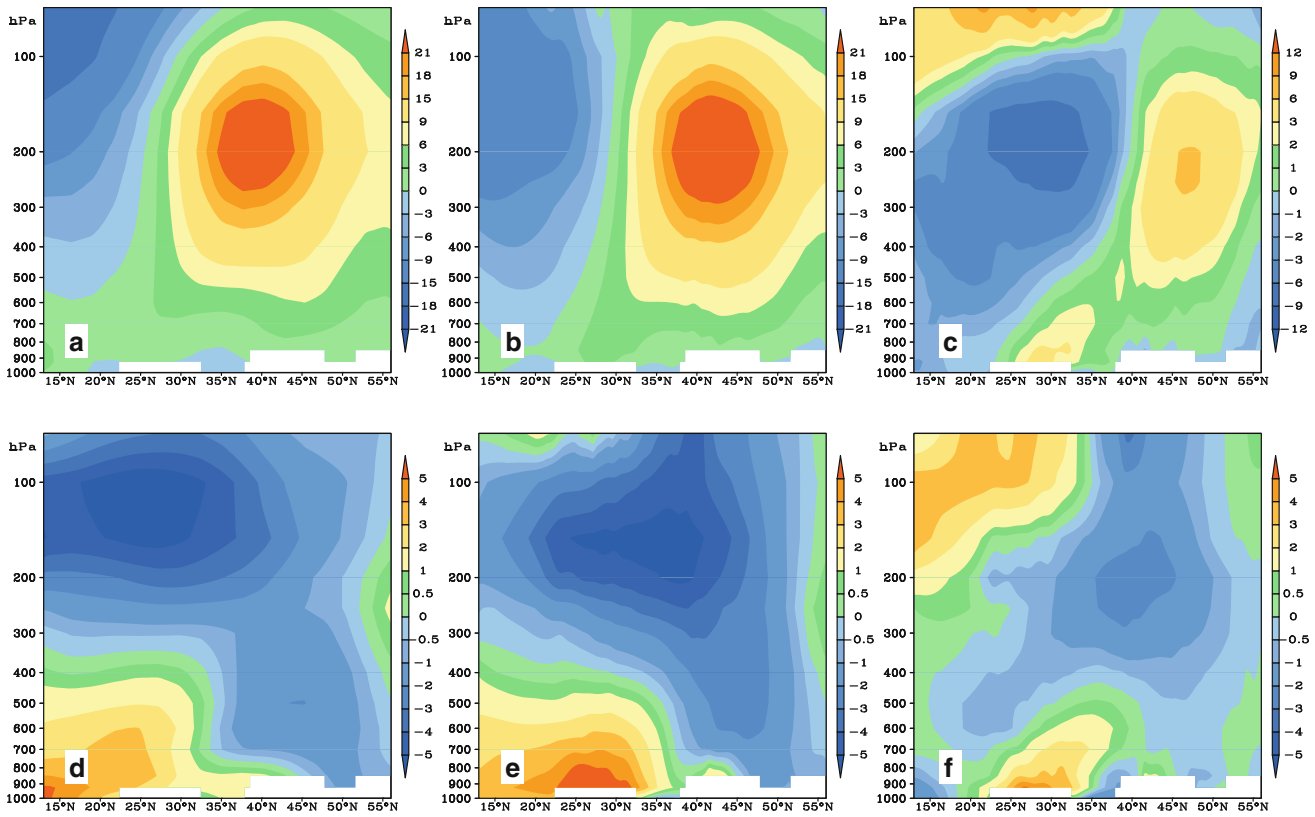

Fig. 12 The pressure-latitude cross-section along the 115°E axis (*white areas* for topography) for the zonal (**a**–**c**) and meridional winds (**c**–**e**) in the summer between the observed (NCEP) data (**a**, **d**) and simulated results (**b**, **e**), and the biases (**c**, **f**, simulated–observed, unit: m s^{-1})

distributions from the southwest to the northeast in the simulated domain. Simulated results are weaker to the south of subtropical westerly jet axis and to the north, which is maximal in northeast Asia. The weaker simulated results to the south of the subtropical westerly jet axis correspond to the stronger simulated EASM.

3.6.1.4 Wind at 850 hPa For the zonal winds at 850 hPa (Fig. 13d–f), a positive bias belt exists from southeast China to Japan. In the Indian subcontinent, the bias is positive in the south and negative in the north. However, the opposite is observed in the Indo-China Peninsula, which is positive in the north and negative in the south. Compared with NCEP reanalysis data, simulated easterly winds from the western Pacific in the low latitudes extend far westward with greater intensity, while simulated westerly winds from the Indian subcontinent to the Indo-China Peninsula retreat westward with less intensity. As a result, a negative bias belt exists in the low latitudes.

For the meridional winds at 850 hPa (Fig. 13g–i), the simulated southerly winds in southeast China are considerably stronger than the observed winds. With the simulated stronger westerly winds (Fig. 13e), there is a positive bias for southwesterly flow in southeast China. The model underestimates southerly winds in the northwest while overestimating northerly winds in the other subregions in the Indian subcontinent. Southerly winds with a negative bias exist for the Indo-China Peninsula. The simulated southerly winds over East China Sea are weaker than the observed winds.

At 850 hPa, the Indian subcontinent is mainly controlled by westerly winds from the Arabian Sea, which transfer to southwesterly flow over the Bay of Bengal (Fig. 13j–l). The flow covers the Indo-China Peninsula and South China Sea and converges with southeasterly flow from the western side of the subtropical high in the western Pacific. Therefore, southwesterly flow exists in southeast China, as well as in the East China Sea and Japan. The model can reproduce the flow distribution accurately. However, obvious biases can be found. Simulated results are much stronger in the southern and northern parts of the Indian subcontinent, while weaker in the middle part. In the Indo-China Peninsula, the bias distribution is different between the south and north, being negative and positive, respectively. In the EASM subregions, the bias distribution is controlled by southwesterly flow from southwest China, the northern Indo-China Peninsula, the SCS, southeast China and Japan. Due to the simulated weaker westerly winds and stronger easterly winds in the low latitudes (Fig. 13f), simulated transferred southerly winds from the

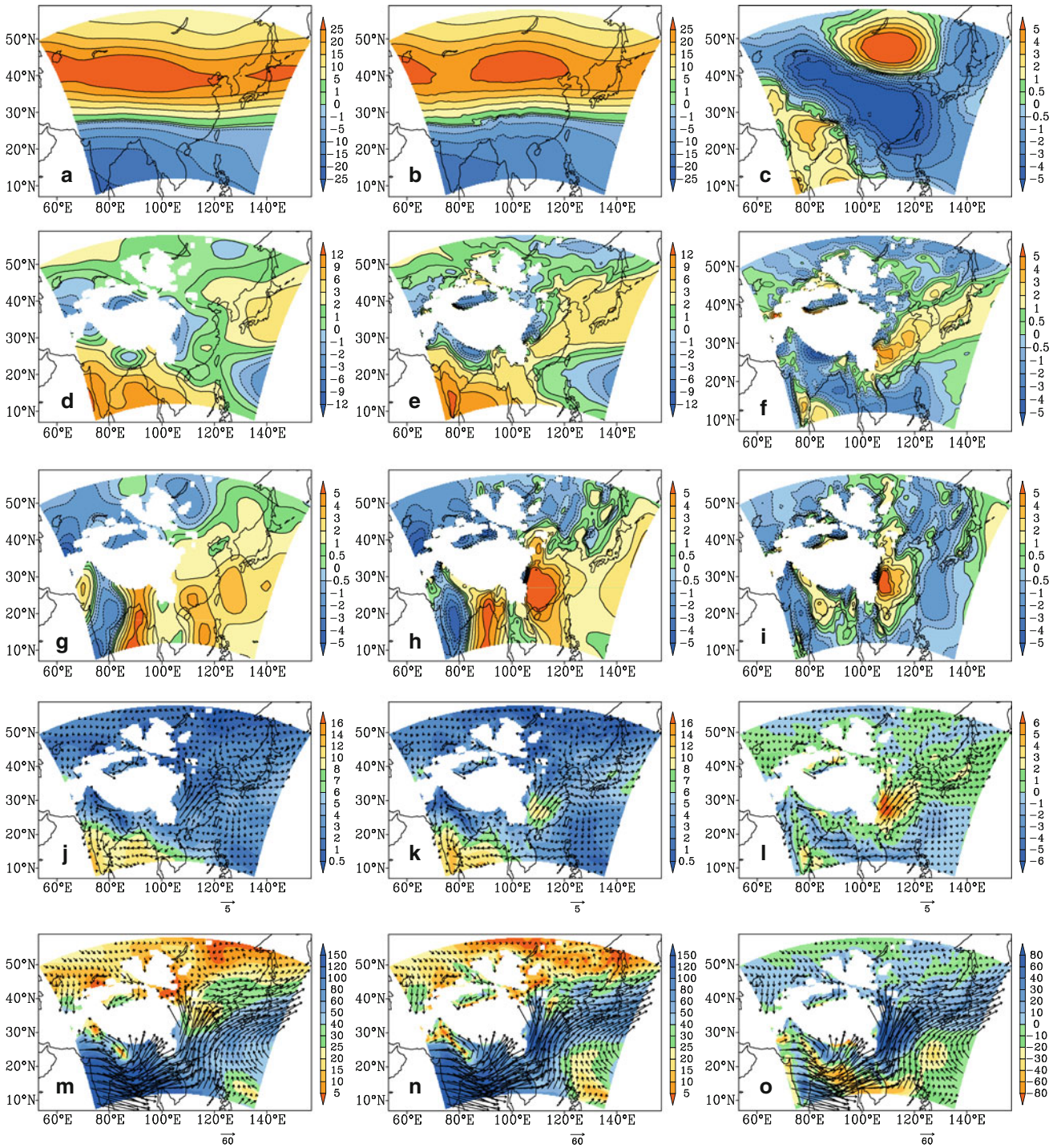

Fig. 13 The spatial distributions (*white areas* for topography above 850 hPa)of the average subtropical westerly jet (**a**–**c**, unit: m s^{-1}), zonal winds (**d**–**f**, unit: m s^{-1}), meridional winds (**g**–**i**, unit: m s^{-1}), wind speed (*shaded*) and vector (**j**–**l**, unit: m s^{-1}), and moisture flux (*shaded*) and vector (**m**–**o**, unit: 10^{-4} kg hPa^{-1} m^{-1} s^{-1}) at 850 hPa in the summer between 1979 and 2008 [**a**, **d**, **g**, **j**, **m** observed, **b**, **e**, **h**, **k**, **n** simulated, **c**, **f**, **i**, **l**, **o** bias (simulated–observed)]

South China Sea to southeast China are stronger (Fig. 13i) and lead to stronger southwesterly flow in southeast China. This corresponds to stronger simulated EASM. Furthermore, simulated southwesterly flow expresses greater intensity with narrow east–west coverage, in which southwesterly winds are observed to the east of Taiwan, while easterly or southeasterly winds are predicted from the simulation. Meanwhile, simulated easterly or

southeasterly winds are weaker in the western Pacific. As a result, the bias at 850 hPa displays an anticyclone circulation characteristic to the southeast of Taiwan over the western Pacific.

3.6.1.5 Moisture transport at 850 hPa For moisture transport at 850 hPa (Fig. 13m–o), the narrowed southwesterly flow over the western Pacific results in stronger moisture transport in the central part of eastern China, which displays a strong positive center and has a significant effect on the precipitation simulations for both the location and intensity. The precipitation is overestimated in northern China and underestimated in southeast China. Meanwhile, the bias is negative for moisture transport in the low latitudes, exhibiting less moisture transport from the southern part of the southwesterly flow and the western Pacific. The stronger moisture transport in the EASM mainly comes from the SCS and the northern part of the southwesterly flow from the Bay of Bengal. The main difference between the simulated and observed data lies in the more strongly simulated moisture center in southeast China, the expanded weak simulated moisture coverage in the western Pacific, and the failure for the model to display a strong moisture center over the Indo-China Peninsula.

3.6.2 In winter

3.6.2.1 PWAT and specified humidity For PWAT (Fig. 14a–c), a negative bias occurs to the south of the Yellow River Valley in eastern China and extends to the Indo-China Peninsula, as well as the southern and western edges of the Tibetan Plateau. The bias is positive in the Indian subcontinent, northern China and Central Asia.

For specific humidity at 850 hPa (Fig. 14d–f), the bias is mainly negative from southeast China to the Indo-China Peninsula, centering in the Indo-China Peninsula. However, the bias is positive in India.

3.6.2.2 Pressure-latitude cross-section for wind fields The pressure-latitude cross-section along the 115°E axis for the zonal and meridional winds in the winter (Fig. 15) is analyzed to determine the model's performance in East Asian winter monsoon simulations.

The zonal winds in the winter are nearly always westerly winds across the whole troposphere, except for the easterly winds in the near surface to the south of 35°N. Simulated westerly winds in the middle latitudes are stronger than the observed ones, while weaker than those observed in the low and high latitudes (Fig. 15a–c). The meridional winds are consistently northerly winds in the middle and high latitudes across the entire troposphere, and extend in the near surface layer in the low latitudes. Simulated northerly winds in the low troposphere are stronger than the observed ones (Fig. 15d–f).

3.6.2.3 Subtropical westerly jet Simulated results along the subtropical westerly jet axis are weaker than the observed data, with the bias being negative in Japan, southeast China and the northern Indian subcontinent (Fig. 16a–c). However, simulated results from northwest China to Central Asia are greater, which correspond to stronger East Asian winter monsoons (EAWM).

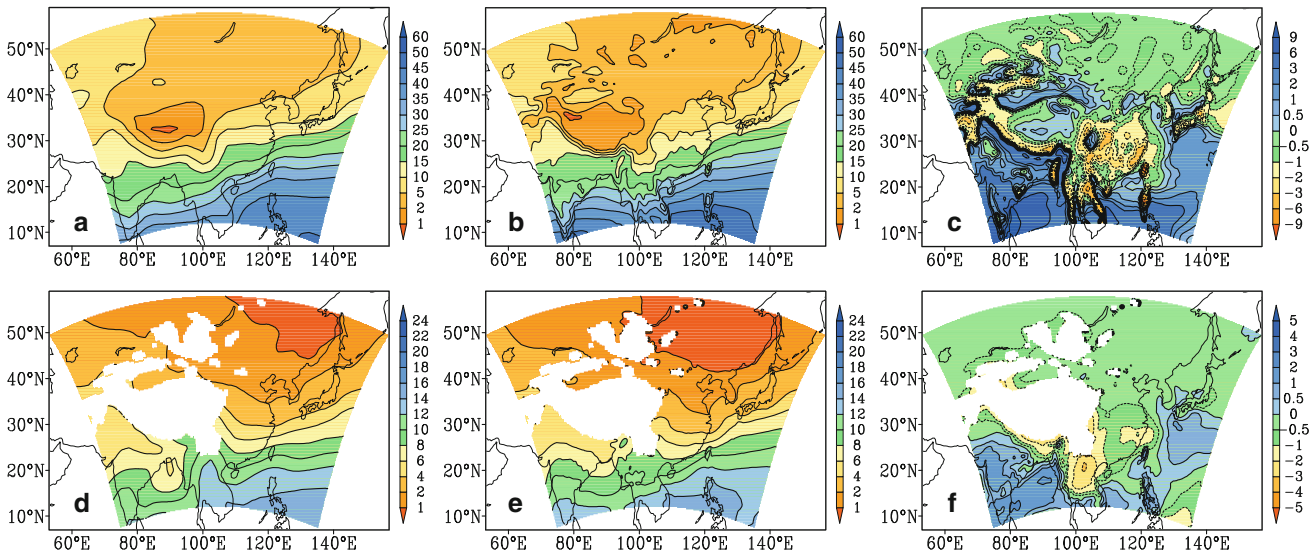

Fig. 14 The spatial distributions of average precipitable water (**a**–**c** unit: cm) and specified humidity (**d**–**f**, unit: 10^{-3} kg kg^{-1}) at 850 hPa (*white areas* for topography above 850 hPa) in the winter between 1979 and 2008 [**a**, **d** observed, **b**, **e** simulated, **c**, **f** bias (simulated–observed)]

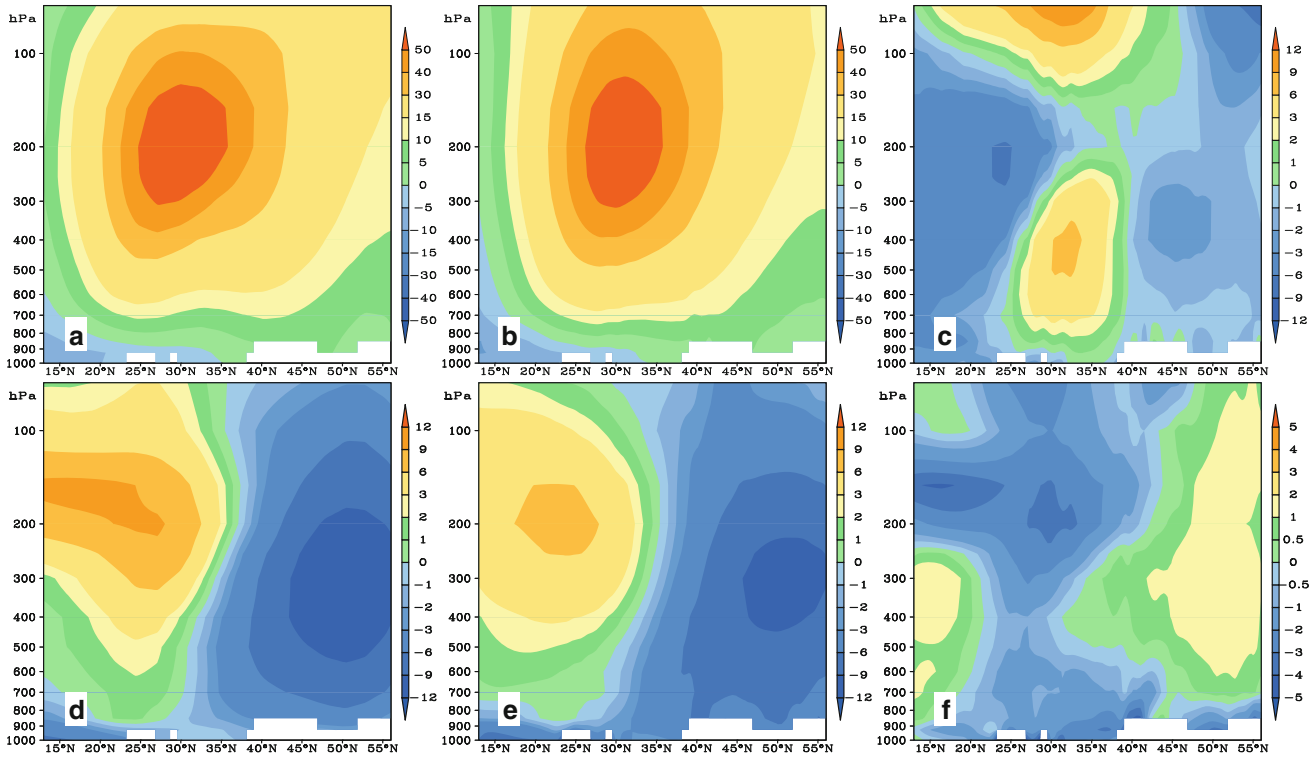

Fig. 15 The pressure-latitude cross-section along the 115°E axis (*white areas* for topography) for the zonal (**a**–**c**) and meridional winds (**c**–**e**) in the winter between the observed (NCEP) data (**a**, **d**) and simulated results (**b**, **e**), and the biases (**c**, **f** simulated–observed, unit: m s^{-1})

3.6.2.4 Wind at 850 hPa For zonal winds at 850 hPa (Fig. 16d–f), simulated results for the westerly winds in the middle latitudes are strong. However, the bias is negative from the Indo-China Peninsula to the Indian subcontinent, due to the northward extension of the easterly winds in the low latitudes. It is worth of noting that there exists a positive bias to the south of the Tibetan Plateau, which extends to southwest China.

There is a negative bias for meridional wind at 850 hPa (Fig. 16g–i) from eastern China to the Indo-China Peninsula, indicating simulated stronger northerly winds in the north and weaker southerly winds in the south. Additionally, the bias is positive in the Indian subcontinent.

At 850 hPa, the winds are controlled by northwesterly flow in Northeast Asia that transfers into two branches, one to westerly winds and the other to northeasterly winds (Fig. 16j–l). The winds are mainly easterly winds from the western Pacific in the low latitudes, which also transfer into two branches in the SCS, one to southwesterly winds and the other continuing as easterly winds. The model can predict the flow in Northeast Asia. However, the bias is positive for the northwesterly winds over northern and eastern China, indicating stronger simulated EAWM. In the low latitudes, the bias is positive, which corresponds to stronger simulated easterly winds. Notably, the simulated easterly winds over the Indo-China Peninsula are stronger with their location extending northward, which results in weaker transfer of southwesterly flow with narrowed east–west coverage in southeast China. Therefore, with stronger simulated EAWM, the transferred northeasterly winds are also stronger. These northeasterly winds, combined with easterly winds from the western Pacific in the Philippines, intensify the easterly flow to the Indo-China Peninsula and the Indian subcontinent, and weaken the moisture transport to southeast China. Additionally, the observed westerly winds to the south of the Tibetan Plateau transfer into two branches in northeast India: one to southwesterly flow over the Bay of Bengal and the other to northeasterly winds along the seashore of the Indian subcontinent. The former flow is described by the model with greater intensity, while the latter fails to be shown.

3.6.2.5 Moisture transport at 850 hPa For moisture transport at 850 hPa (Fig. 16m–o), the observed strong easterly moisture transport is mainly located to the east of the Indo-China Peninsula in the low latitudes. The flow transfers into two branches: one continues westward and the other turns northward in the SCS and the Indo-China Peninsula, from which a large amount of moisture is transported to eastern China. However, simulated results show that easterly moisture transport extends far westward to the southern Indian subcontinent with the location

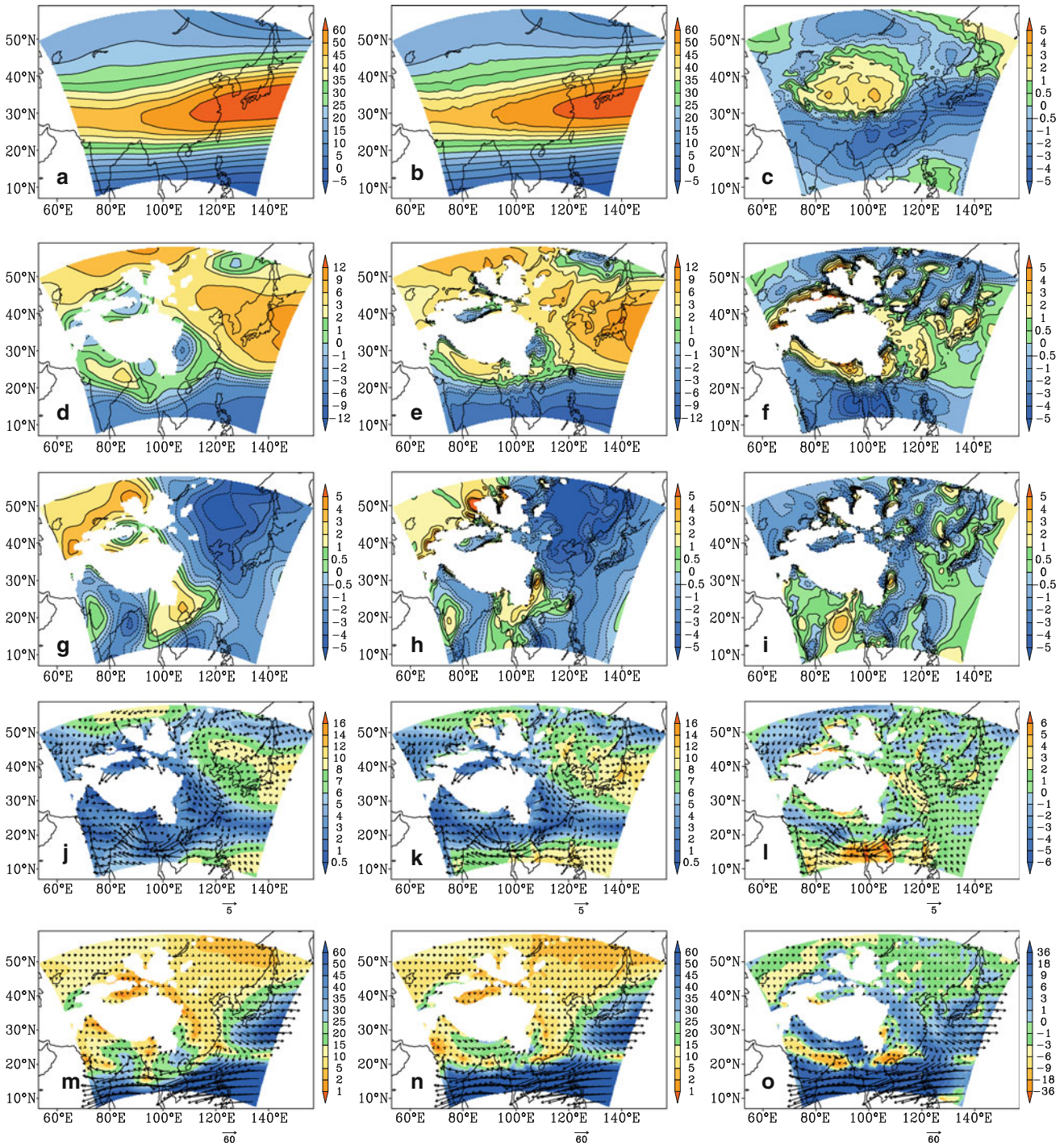

Fig. 16 The spatial distributions (*white areas* for topography above 850 hPa) of the average subtropical westerly jet (**a–c** unit: m s^{-1}), zonal winds (**d–f** unit: m s^{-1}), meridional winds (**g–i** unit: m s^{-1}), wind speed (*shaded*) and vector (**j–l** unit: m s^{-1}), and moisture flux (*shaded*) and vector (**m–o** unit: 10^{-4} kg hPa^{-1} m^{-1} s^{-1}) at 850 hPa in the winter between 1979 and 2008 [**a**, **d**, **g**, **j**, **m** observed, **b**, **e**, **h**, **k**, **n** simulated, **c**, **f**, **i**, **l**, **o** bias (simulated–observed)]

expanding northward. The results are in weaker the southern branch of the southwesterly winds and less moisture transport to eastern China is observed; in contrast greater moisture transport to the Indian subcontinent and the Indo-China Peninsula is predicted based on higher simulated precipitation levels in those areas. Additionally, due to the failure of the model to reproduce the transfer of the flow from southwesterly winds to northeasterly winds in northeast India, the northern branch of the southwesterly winds in northern India is stronger. This strengthens

moisture transport and increases precipitation to southwest China. The weakened southern branch of the southwesterly moisture transport, combined with weakened transferred southerly winds from the western Pacific and the SCS, result in less precipitation in southeast China. Additionally, strengthened easterly moisture transport in the low latitudes from the western Pacific leads to greater moisture transport and increased precipitation to the Indo-China Peninsula and the Indian subcontinent.

4 Conclusions and discussion

The model can generally reproduce the distributions of precipitation, which is greater in the south and decreases in the north. However, the model overestimates precipitation in the Tibetan plateau and in northeastern Asia, as well as in the southern subregions of the Indian subcontinent and in the Indo-China Peninsula. Additionally, precipitation is underestimated in Central Asia. The model underestimates precipitation in southern China, where a negative bias in the annual and winter simulations is observed; this bias extends westward to southwestern China in the summer.

In terms of the correlation between the observed and simulated spatial distributions of precipitation, the model performs well in northeastern Asia and in the eastern Tibetan plateau, as well as in the Indo-China Peninsula and the northern Indian subcontinent. However, the subregions north of the Tibetan plateau display less correlation and greater RRMSE values. Daily and monthly mean precipitation can be reproduced accurately by the model. Simulated upper and root soil water correlate well with remote sensing derived soil moisture.

The model captures the annual variations in averaged precipitation and its anomalies in East Asia, as well as the subregions with different precipitation intensities. Further analysis within the three subregions shows that the model generally captures rain belt movement in the low latitudes, which are closely connected with the EAM and IM as well rain belt movement in the Indo-China Peninsula. The distribution of the rain belt in the north is also reproduced by the model well. However, the relative bias in the north is greater, with wider coverage than that observed in the south for both SR1 and SR2. The relative bias in the winter is stronger than that in the summer.

The model can generally grasp the major anomalies in interannual variation of precipitation in East Asia, as well as the subregions with different precipitation intensities. Further analysis of the simulated and observed data for the three subregions shows that the model performs well in capturing the average precipitation and its anomalies. However, differences in the bias distributions can be found between the different subregions. There is a greater relative positive bias in the north that in the south for both SR1 and SR3, while a greater bias between 36 and 39°N is observed in SR2.

In general, the model simulates precipitation well. The simulated precipitation is 26 % greater than observed precipitation in East Asia and 18, 34 and 26 % greater than the observed precipitation in the three subregions, SR1, SR2, and SR3, respectively.

Differences between the simulated and observed precipitation in the summer can be summarized as follows. With the stronger simulated subtropical westerly jet accompanied by the jet axis moving northward, the simulated EASM is stronger than the observed. The channel for simulated moisture transport from southwesterly flow is narrower than observed; additionally, easterly flow from the western Pacific extends westward. Moisture transport from the western Pacific and the southern branch of the southwesterly winds from the Bay of Bengal are weakened in the simulation. The strengthened moisture transport in eastern China comes from the SCS and the northern branch of the southwesterly flow from the Bay of Bengal. The precipitation bias in eastern China displays the opposite distribution, being negative in the south and positive in the north. In the Indian subcontinent, precipitation is overestimated in the northwest and the south. In the Indo-China Peninsula, there is less positive bias in the southwest and a greater negative bias in the northeast, which is connected with the strong negative bias in southwest China.

Differences between the simulated and observed precipitation in the winter can be summarized as follows. With the stronger simulated westerly winds in the middle latitudes and the stronger simulated northerly winds in the low troposphere, the simulated EAWM is also stronger than the observed. Additionally, with the stronger easterly flow in the low latitudes, moisture transport to the Indian subcontinent and the Indo-China Peninsula from the western Pacific and the SCS is stronger in the simulation. However, simulated moisture transport from the Bay of Bengal (southern branch of southwesterly moisture transport), as well as transferred southerly flow from the SCS and the Indo-China Peninsula, is weaker than the observed, which results in less simulated moisture transport to eastern China. Meanwhile, due to the failure to simulate the transfer from northwesterly to northeasterly winds in northeast India, simulated southwesterly winds in northern India re stronger (northern branch of southwesterly winds). As a result, there is a strong negative bias for the precipitation in southern China and a positive bias in India, the Indo-China Peninsula and southwest China.

RIEMS can generally reproduce the rainfall belt movement, daily and monthly mean precipitation, as well as annual and interannual variation. However, there are biases between the observations and the simulation, which

is a common difficulty from RCMs and GCMs. The difference for the wind field between the NCEP reanalysis data and simulated results shows that climate drift during long-time consecutive integration exists. Consecutive integrations with frequent re-initializations, as well as 3D-nudging, are a good approach to improve the accuracy of RCMs (Lo et al. 2008). Meanwhile, RCMs depend on GCMs or analysis data as driven data for initial and boundary conditions. Error from driven data can be involved in the simulated results from RCMs. Nudging with observed data can adjust the bias between the simulated results and the observed data. Multidriven data is another method to decrease the origin of the bias.

Due to the scarcity of the observed data and the computing capacity, the present common spatial resolution for RCMs is not enough to resolve actual atmospheric conditions and different parameterization schemes are adopted by the regional climate models. For example, there is an obvious inconsistency from the different cumulus parameterization schemes for the regional applicability of RCMs. Ensemble simulations can decrease the model's uncertainty (Zhao and Fu 2010). Meanwhile, some parameters are considered unchanged when performing long term integration for current RCMs. For example, land use/cover change can alter the surface albedo and then change the energy and water cycles between the land surface and the atmosphere. This will have an effect on local and regional climate.

Several factors result in the poor performance of RCMs for some seasons and regions. However, compared to GCMs, high-resolution RCMs can describe topography, land-sea distributions and surface vegetation more accurately, as well as show regional characteristics in East Asia. With the Tibetan Plateau and desert in the southwest and northwest, as well as the Pacific in the east, topographic distributions in China are complex. There have been significant effects from anthropogenic forcing with regard to land use, vegetation cover and aerosol emissions in recent years. Improvements in computing capacity make high-resolution RCMs possible, for which finer forcing data, such as land use and vegetation data from remote sensing, can be used to improve the model's description of land surface characteristics and disclose its effect on regional climate. It is crucial to involve all of these factors and ensure that they are captured by the RCMs. Based the present analysis of RIEMS's performance on regional climate simulations over East Asia, the biological, human, and chemical components will be coupled with the natural monsoon system to make it a physically, biologically, chemically and socially coupled system.

As a result, the failure for physical process to be accurately expressed in RCMs is the main difficulty for model development and accounts for the main bias of the model. However, current RCMs usually fail to express the component in the 'General Monsoon System' and cannot correctly disclose the feedback between climate and ecosystem. This problem can be solved with effort, which is the initial aim for RIEMS development.

Acknowledgments The author would like to thank all researchers involved in the development of RIEMS from the Key Laboratory of Regional Climate-Environment for East Asia (RCE-TEA) and Nanjing University. This work was supported by the National Basic Research Program of China (973) under grant No. 2011CB952003, Chinese Academy of Sciences Strategic Priority Program under grant No. XDA05090206 and the National Natural Science Foundation of China under grant No. 40975053. I thank the reviewers for their numerous valuable comments to improve the manuscript.

References

Afiesimama EA, Pal JS, Abiodun BJ, Gutowski WJ, Adedoyin A (2006) Simulation of west Africa monsoon using the RegCM3. Part I: model validation and interannual variability. Theor Appl Climatol 86:23–37

Annamalai H, Slingo JM, Sperber KR, Hodges K (1999) The mean evolution and variability of the Asian summer monsoon: comparison of ECMWF and NCEP–NCAR reanalyses. Mon Weather Rev 127:1157–1185

Briegleb BP (1992) Delta-Eddington approximation for solar radiation in the NCAR Community Climate Model. J Geophys Res 97:7603–7612

Ceballos A, Scipal K, Wagner W, Martínez-Fernández J (2005) Validation of ERS scatterometer-derived soil moisture data in the central part of the Duero Basin, Spain. Hydrol Process 19:1549–1566

Dickinson RE, Errico RM, Giorgi F, Bates GT (1989) A regional climate model for the western United States. Clim Change 15:383–422

Dickinson RE, Henderson-Sellers A, Kennedy PJ (1993) Biosphere-atmosphere transfer scheme (BATS) Version1e as coupled to the NCAR Community Climate Model. Technical report NCAR/TN-387_STR.1993

Ding YH, Zhang J, Zhao ZC (1998) An improved land-surface processes model and its simulation experiment Part II: land-surface processes model (LPM-ZD) and its coupled simulation experiment with regional climate model. Acta Meteor Sin 56:385–399 (in Chinese)

Drusch M, Wood EF, Gao H, Thiele A (2004) Soil moisture retrieval during the Southern Great Plains hydrologic experiment 1999: a comparison between experimental remote sensing data and operational products. Water Resour Res 40:W02504. doi: 10.1029/2003WR002441

Dudhia J, Gill D, Guo YR, Manning K et al. (2001) PSU/NCAR mesoscale modeling system tutorial class notes and users' guide (MM5 modeling system version 3), NCAR/MMM

Forster P, Ramaswamy V, Artaxo V, Berntsen T, Betts R, Fahey DW, Haywood J, Lean J, Lowe DC, Myhre G, Nganga J, Prinn R, Raga G, Schulz M, Van Dorland R (2007) Changes in atmospheric constituents and in radiative forcing. In: Solomon S, Qin D, Manning M, Chen Z, Marquis M, Averyt KB, Tignor M, Miller HL (eds) Climate change 2007: the physical science basis. Contribution of Working Group I to the fourth assessment report of the Intergovernmental Panel on Climate Change. Cambridge University Press, Cambridge

Fu CB (1997) Concept of "general monsoon system", an earth system science view on Asia monsoon. In: Proceedings of the international workshop on regional climate modeling of the general monsoon system in Asia, Beijing, China, pp 1–6

Fu CB, Wei HL, Qian Y, Chen M (2000) Documentation on regional integrated environmental model system (RIEMS version 1). TEACOM science reports START Regional Committee for temperate East Asia, TSR.2000

Fu CB, Wang SY, Xiong Z, Gutowski WJ, Lee DK, McGregor JL, Sato Y, Kato H, Kim JW, Suh MS (2005) Regional climate model intercomparison project for Asia. Bull Am Meteor Soc 86:257–266

Fu CB, De Varies FWTP, Ai LK,Chen CTA, Lebel L, Manton M, Snidvongs A, Virji H (2006) The initial science plan of the monsoon Asia integrated regional study. MAIRS-IPO, IAP-CAS, P.O.Box9804, 100029 Beijing, China (80 pp)

Gao XJ, Zhao ZC, Ding YH, Huang RH, Giorgi F (2001) Climate change due to greenhouse effects in China as simulated by a regional climate model. Adv Atmos Sci 18:1224–1230

Gao XJ, Xu Y, Zhao ZC, Pal JS, Giorgi F (2006) On the role of resolution and topography in the simulation of East Asia precipitation. Theor Appl Climatol 86:173–185

Giorgi F, Bates GT (1989) The climatological skill of a regional model over complex terrain. Mon Weather Rev 117:2325–2347

Giorgi F, Mearns LO (1999) Introduction to special section-regional climate modeling revisited. J Geophys Res 104(D6):6335–6352

Giorgi F, Marinucci MR, Bates GT (1993a) Development of a second-generation regional climate model (RegCM2). Part I: boundary-layer and radiative transfer processes. Mon Weather Rev 121:2794–2813

Giorgi F, Marinucci MR, Bates GT, Canio GD (1993b) Development of a second generation regional climate model (RegCM2). Part II: convective processes and assimilation of lateral boundary conditions. Mon Weather Rev 121:2814–2832

Giorgi F, Bi XQ, Pal JS (2004) Mean, interannual variability and trends in a regional climate change experiments over Europe. I. Present-day climate (1961–1990). Clim Dyn 22:733–756

Giorgi F, Coppola E, Solmon F, Mariotti L et al (2012) RegCM4: model description and preliminary tests over multiple CORDEX domains. Clim Res 52:7–29

Grell GA, Dudhia J, Stauffer DR (1995) A description of the fifth-generation Penn State/NCAR mesoscale model (MM5). Technical report NCAR/TN-398_STR.1995

Jacob D, Andrae U, Elgered G, Fortelius C, Graham LP, Jackson SD, Karstens U, Koepken CHR, Lindau R, Podzun R, Rockel B, Rubel F, Sass HB, Smith RND, Van den Hurk BJJM, Yang X (2001) A comprehensive model intercomparison study investigating the water budget during the BALTEX-PIDCAP period. Meteorol Atmos Phys 77:19–43

Kain JS, Fritsch JM (1993) Convective parameterization for mesoscale models: the Kain-Fritsch scheme. The representation of cumulus convection in numerical models. In: Emanuel KA, Raymond DJ (eds) Am Meteorol Soc 165–170

Kiehl JT, Hack JJ, Bonan GB, Boville BA, Briegleb BP, Williamson DL, Rasch PJ (1997) Description of the NCAR community climate model (CCM3). Technical report NCAR/TN-420_STR.1997

Liu XD, Jiang ZH, Luo SR, Zhang XM, Li AH, Cheng Z (2005) A simulation of summer precipitation over eastern China with RegCM3. J Nanjing Inst Meteor 28:351–359 (in Chinese)

Liu SY, Liang XZ, Gao W, Zhang H (2008) Application of climate-weather research and forecasting model (CWRF) in China: domain optimization (in Chinese). Chin J Atmos Sci 32:457–468

Lo JCF, Yang ZL, Pielke R Sr (2008) Assessment of three dynamical climate downscaling methods using the Weather Research and Forecasting (WRF) model. J Geophys Res 113:D09112. doi:10.1029/2007JD009216

Njoku E (2004) (updated daily) AMSR-E/aqua daily L3 surface soil moisture, interpretive parameters, & QC EASE-Grids V002, [June to August, 2002–2008]. National Snow and Ice Data Center. Digital media, Boulder

Pal JS, Giorgi F, Bi XQ, Elguindi N, Solmon F, Gao XJ, Francisco R, Zakey A, Winter J, Ashfaq M, Syed FS, Sloan LC, Bell JL, Diffenbaugh NS, Karmacharya J, Konaré A, Martinez D, Rocha RPA, Steiner AL (2007) Regional climate modeling for the developing world: the ICTP RegCM3 and RegCNET. Bull Am Meteorol Soc 88:1395–1409

Roeckner E, Arpe K, Bengtsson L, Christoph M, Claussen M, Dümenil L, Esch M, Giorgetta M, Schlese U, Schulzweida U (1996) The atmospheric general circulation model ECHAM-4: model description and simulation of the present day climate. Max-Planck-Institut für Meteorologie report no. 218

Rudolf B, Becker A, Schneider U, Meyer-Christoffer A, Ziese M (2010) The new "GPCC full data reanalysis version 5" providing high-quality gridded monthly precipitation data for the global land-surface is public available since December 2010, Global Precipitation Climatology Centre (GPCC). DWD, Internet publication, pp 1–7. Available online at http://gpcc.dwd.de

Schneider U, Becker A, Meyer-Christoffer A, Ziese M, Rudolf B (2010) Global precipitation analysis products of the GPCC. Global Precipitation Climatology Centre (GPCC). DWD, Internet publication, pp 1–12. Available online at http://gpcc.dwd.de

Skamarock WC, Klemp JB, Dudhia J, Gill DO, Barker DM, Wang W, Powers JG (2005) A description of the advanced research WRF version 2. Technical report NCAR/TN-468_STR.2005

Skamarock WC, Klemp JB, Dudhia J, Gill DO, Barker DM, Duda MG, Wang W, Powers JG (2008) A description of the advanced research WRF Version 3. Technical report NCAR/TN-475_STR.2008

Tang JP, Su BK, Zhao M, Zhao DM (2006) Numerical simulation of long-term climate change in East Asia. Acta Meteorol Sin 20(1):50–61

Wagner W, Lemoine G, Borgeaud M, Rott H (1999) A study of vegetation cover effects on ERS scatterometer data. IEEE Trans Geosci Remote Sens 37:938–948

Wagner W, Naeimi V, Scipal K, Dejeu R, Martinez-Fernandez J (2007) Soil moisture from operational meteorological satellites. Hydrogeol J 15:121–131. doi:10.1007/s10040-006-0104-6

Wang B, Lin H (2002) Rainy season of the Asian–Pacific summer monsoon. J Clim 15:386–398

Yu RC (1989) Design of the limited area numerical weather prediction model with steep mountains. Chin J Atmos Sci 13:139–149 (in Chinese)

Zhang DF, Ouyang LC, Gao XJ, Zhao ZC, Pal JS, Giorgi F (2007) Simulation of the atmospheric circulation over East Asia and climate in China by RegCM3. J Trop Meteor 23:444–452 (in Chinese)

Zhao DM, Fu CB (2009) Comparisons on RIEMS2.0's ability to simulate multi-year mean climate in northern China with two model domains. Atmos Oceanic Sci Lett 2:386–391

Zhao DM, Fu CB (2010) The analysis on the ability of RIEMS2.0 (Regional Integrated Environment Modeling System) to simulate two extreme climate events in the summer of 1997/98 in China. Acta Meteor Sin 68:325–338 (in Chinese)

Zhao ZC, Luo Y (1998) Advance on investigations of regional climate modeling since 1990. Acta Meteor Sin 56:225–246 (in Chinese)

Zhao DM, Su BK, Zhao M (2006) Soil moisture retrieved from satellite images and its application to heavy rainfall simulation in Eastern China. Adv Atmos Sci 23:299–316

Zhao DM, Kuenzer C, Fu CB, Wagner W (2008) Evaluation of the ERS scatterometer derived soil water index to monitor water availability and precipitation distribution at three different scales in China. J Hydrometeorol 9(3):549–562

Zhao DM, Fu CB, Yan XD (2009) Testing the ability of RIEMS2.0 (Regional Integrated Environment Modeling System) to simulate multi-year precipitation and air temperature in China. Chin Sci Bull 54:3101–3111. doi:10.1007/s11434-009-0178-3